THE BALTIC JOURNAL
OF ROAD AND BRIDGE ENGINEERING
2025/20(4)

ISSN 1822-427X/eISSN 1822-4288
2025 Volume 20 Issue 4: 106–133
https://doi.org/10.7250/bjrbe.2025-20.668

MULTISCALE EVALUATION OF OPEN-GRADED FRICTION COURSE (OGFC) ASPHALT MIXTURE FATIGUE DAMAGE

BAOYANG YU[1], ZHIZHANG ZHOU[1], CHUNSHUAI ZHANG[2], LIN QI[3*]

[1]*School of Transportation and Geomatics Engineering, Shenyang Jianzhu University, Shenyang, China*

[2]*Hydrochina Huadong Engineering Corporation, Hangzhou, China*

[3]*Department of Civil Engineering, Shenyang Urban Construction University, Shenyang, China*

Received 12 February 2025; accepted 10 November 2025

Abstract. Research on the microscopic mechanisms of open-graded friction courses (OGFCs) is still in its early stages, and the specific effects of various factors on the fatigue performance of OGFCs have not been fully explored. This study investigates the effects of oil-stone ratios, void fractions, and maximum nominal particle sizes on the fatigue life of OGFCs at the macroscopic and microscopic scales. At the macroscopic level, indirect tensile fatigue tests were conducted on OGFC specimens. At the microscopic level, a three-dimensional (3D) reconstruction model of OGFC was developed using computed tomography (CT) and image processing techniques. Additionally, a 3D randomized aggregate model was developed using the Monte Carlo method and an aggregate random placement algorithm. Virtual splitting and fatigue tests were conducted to analyse the correlation between virtual and experimental macroscopic tests. The results showed that the splitting strength and fatigue life of the OGFC increased at higher oil-stone ratios but decreased at higher void fractions and larger nominal

* Corresponding author. E-mail: qilin6126@126.com

Baoyang YU (ORCID ID 0000-0002-5826-7248)
Zhizhang ZHOU (ORCID ID 0009-0000-8978-1111)
Lin QI (ORCID ID 0000-0001-9268-6924)

maximum particle sizes. The variation in the results of the virtual splitting fatigue tests derived from the CT reconstruction model and the experimental results was only 9–11%, indicating a strong correlation between the two approaches.

Keywords: asphalt mixture, CT reconstruction, fatigue damage, numerical simulation, multiscale analysis, open-graded friction course.

Introduction

Fatigue damage is a failure phenomenon caused by the gradual expansion of internal defects in a material under load cycling (Lv et al., 2023). As a typical open-graded asphalt mixture with large voids, an open-graded friction course (OGFC) features a point-to-point support structure that induces repeated stress concentrations within the internal material under cyclic loading conditions. These stress concentrations result in fatigue damage, primarily manifested as crack initiation and propagation (Manrique-Sanchez et al., 2020; Song et al., 2021). Consequently, OGFC asphalt pavements are more vulnerable to external influences than other pavements (Wu et al., 2021; Zhang et al., 2020a).

Recently, researchers have extensively studied the fatigue performance of asphalt mixtures using phenomenological methods, leading to the development of various fatigue models (Fan et al., 2022a; Fan et al., 2022b; Ipekyol et al., 2022; Wang et al., 2023). Some researchers have also investigated the strength degradation of asphalt mixtures through fatigue tests. Currently, two large-scale outdoor fatigue test methods are available, namely, the American Association of State Highway and Transportation Officials test (Hadley, 1993) and full-scale pavement accelerated loading test (Chen & Hugo, 1998). However, these methods require significant investment and extended testing durations, making them impractical for widespread applications. Consequently, indoor small-specimen fatigue tests have become the preferred approach owing to their cost-effectiveness, efficiency, and simplicity (Fakhri et al., 2013; Lv et al., 2018; Poulikakos et al., 2014; Sun et al., 2018).

Macroscopic tests primarily focus on the effects of external conditions and mixed properties on the fatigue performance of OGFCs (Jian, 2011). For instance, Song et al. (2016) analysed the bonding between OGFC and various subgrade asphalt mixtures using shear fatigue tests, concluding that fatigue performance correlates with the contact area between the OGFC and its substrate. Muniandy et al. (2004) demonstrated that incorporating 0.4–0.7% fibre content by weight significantly enhances the fatigue strength of the OFGC and delays crack formation and propagation. Zhang et al. (2020b) employed four-point bending fatigue tests to evaluate the effects of increased SBS asphalt content on OGFC fatigue performance, revealing that increased SBS dosage improves fatigue resistance.

While small-specimen tests effectively evaluate strength evolution, cracking, and deformation behaviour, they are limited to observing macroscopic mechanical changes and cannot provide insights into crack initiation, propagation mechanisms, or the effects of microstructural factors on fatigue life (Jiang et al., 2018; Yu et al., 2020).

To overcome these limitations, many researchers have introduced numerical simulation techniques into virtual testing of asphalt mixtures (Jiang et al., 2021; Liu et al., 2021; Phanden et al., 2022). These types of simulations reproduce mechanical tests in a controlled digital environment, allowing detailed analysis of internal structure evolution and stress distribution under cyclic loading conditions. Common microscopic approaches include computed tomography (CT) combined with digital image processing (Hu et al., 2017; Mackiewicz & Szydło, 2019) and virtual random placement modelling (Wang et al., 2018). For example, Ma et al. (2016) and Wang et al. (2018) applied the discrete element method (DEM) to simulate four-point bending fatigue, revealing that increased void content leads to accelerated crack propagation. Peng et al. (2020) further combined DEM with image processing to quantify the influence of aggregate morphology and gradation on fracture resistance. Li et al. (2019) reconstructed 3D DEM models from CT scans to simulate indirect tensile fatigue, identifying anisotropic particle trajectories caused by non-uniform stress fields. In parallel, Su and Nikraz (2022) integrated the simplified viscoelastic continuum damage theory with numerical modelling to predict fatigue life, and Kim et al. (2008) incorporated viscoelastic damage theory into finite element analysis to evaluate pavement fatigue performance. More recently, Li et al. (2020) and Chen et al. (2023) utilised high-resolution CT imaging to visualize fatigue damage evolution and quantify the effects of aggregate geometry on cracking behaviour.

Despite these advances, research on the microstructural mechanical behaviour of OGFCs remains limited, especially pertaining to the influence of mixture composition on fatigue performance. In recent years, multiscale fatigue modelling and digital reconstruction techniques have been increasingly employed to link microstructural evolution with macroscopic fatigue response. For instance, Chen et al. (2023) and Tan et al. (2024) integrated CT reconstruction with viscoelastic damage models to capture fatigue crack propagation under cyclic loads, whereas Wu et al. (2024) conducted multiscale finite-element analyses to investigate fracture mechanisms at the aggregate–binder interface. Mohamed et al. (2024) further developed a microstructure-based finite element method (FEM) framework to simulate interfacial stress evolution and localized damage. These recent efforts highlight a growing trend toward integrating experimental and numerical methods to enhance the predictive accuracy of fatigue life in porous asphalt systems.

From a multiscale perspective, macroscopic analysis focuses on the overall mechanical response of OGFCs subjected to cyclic loading – such as tensile strength, stiffness degradation, and fatigue life obtained from laboratory tests – whereas

microstructural analysis explores localized stress concentration, void connectivity, and crack propagation within the asphalt-aggregate skeleton using CT-based reconstruction and numerical modelling. This distinction clarifies that macroscopic testing reflects the global performance governed by material composition and boundary conditions, while a microstructural analysis reveals the intrinsic mechanisms of fatigue damage initiation and evolution. Together, they establish a coherent multiscale framework bridging global structural behaviour and internal microstructural response, providing a comprehensive basis for understanding fatigue mechanisms in OGFC mixtures.

Accordingly, this study investigates the influences of oil–stone ratio, void fraction, and nominal maximum particle size on the fatigue behaviour of OGFC mixtures via indirect tensile fatigue tests at the macroscopic level and further simulates the fatigue cracking process from a microstructural perspective using ABAQUS and FESAFE, thereby providing new theoretical insights into the fatigue damage mechanisms of OGFCs.

1. Materials and mix proportions

1.1. Material properties

In this study, basalt was used as coarse and fine aggregates, while limestone mineral powder served as the filler. The physical properties of the aggregates and mineral fillers were tested following the Chinese technical specification "Aggregate Testing Procedure for Highway Engineering" (JTG F42-2005) (China Communications Press, 2005). The results are listed in Table 1.

Liao He 90# asphalt was selected as the base asphalt, and an OLB-1 type high-viscosity modifier was used to prepare the high-viscosity modified asphalt. The OLB-1 modifier is a light-yellow, semi-transparent, hemispherical granular polymer composed of highly dispersed vulcanized styrene-butadiene polymer, tackifiers, and plasticizers at the nanoscale, designed to enhance the cohesion and elasticity of asphalt binders. The performance of the modified asphalt was evaluated according to the "Highway Engineering Asphalt and Asphalt Mixture Test Procedures" (JTG E20-2011) (China Communications Press, 2011). The results are summarized in Table 2.

Table 1. Technical indicators for crude aggregates

Mineral type	Test technical indicator	Unit	Limiting value	Result	Standard method
Coarse aggregate	Crushing value	%	≤26	11.5	T0316
	Los Angeles abrasion loss	%	≤28	19	T0317
	Apparent relative density	–	≥2.6	3.1	T0304
	Water absorption rate	%	≤2	0.14	T0304
	Robustness	%	≤8	6.5	T0314
	Content of needle and flake particles	%	≤10	5.7	T0312
	Soft stone content	%	≤3	0.9	T0320
	Grind value	–	≥40	52	T0321
	Adhesion between coarse aggregate and asphalt with polished value	–	≥5	6.5	T0616
Fine aggregate	Apparent relative density	–	≥2.5	2.65	T0328
	Sand equivalent	%	≥60	70	T0334
	Angularity (flow time)	s	≥30	38.6	T0345
Mineral powder	Apparent relative density	–	≥2.45	2.705	T0352
	Hydrophilic coefficient of mineral powder	–	<1	0.59	T0353
	Water content	–	<1	0.45	T0103

Table 2. Technical indicators of high-viscosity modified asphalt

Test technical indicator	Unit	Limiting value	Result	Standard method
Softening point	°C	>80	95.5	T0606
Penetration, 25 °C	mm	>40	53.6	T0604
Penetration index	–	–	0.85	T0604
Ductility, 5 °C	cm	≥30	32	T0605
Ductility, 15 °C	cm	≥80	129.4	T0605
Ductility viscosity, 60 °C	Pa·s	>20000	30257	T0620

1.2. Mix proportion design

Based on the requirements of Jing and Zhendong (2013), the grading was designed for the OGFC asphalt mixtures with different oil-stone ratios (4.9%, 5.1%, and 5.3%), void fractions (19%, 21%, and 23%), and nominal maximum particle sizes (10, 13, and 16 mm). The results are summarised in Table 3.

Table 3. Grading table of different characteristic factors in open-graded friction courses (OGFCs)

Gradation type		Mesh size, mm											Oil-stone ratio, %	Void fraction, %
		19	16	13.2	9.5	4.75	2.36	1.18	0.6	0.3	0.15	0.075		
Different oil-stone ratios	OGFC-13-4.9 %	100	95	70	15	12	10	8.5	6.5	5	4	4.9	21.21	
	OGFC-13-5.1 %	100	95	70	15	12	10	8.5	6.5	5	4	5.1	20.97	
	OGFC-13-5.3 %	100	95	70	15	12	10	8.5	6.5	5	4	5.3	20.73	
Different void fractions	OGFC-13-19 %	100	96	80	30	12	10	8.5	6.5	5	4	5.1	18.95	
	OGFC-13-21 %	100	95	70	15	12	10	8.5	6.5	5	4	5.1	20.97	
	OGFC-13-23 %	100	90	70	14	12	10	8.5	6.5	5	4	5.1	22.95	
Different nominal maximum particle sizes	OGFC-10		100	95	55	12	10	8.5	6.5	5	4	5.3	16.54	
	OGFC-13		100	95	70	15	12	10	8.5	6.5	5	4	5.1	20.97
	OGFC-16	100	95	80	57.5	15	12	10	8.5	6.5	5	4	4.9	23.68

In this study, we designed OGFCs with varying oil–stone ratios, void fractions, and nominal maximum particle sizes, all maintaining the same gradation in the 0–2.36 mm particle-size range. The specific surface area method was employed, allowing the determination of oil-sand ratios for different asphalt mortars using Equations (1) and (2), along with the surface area coefficient (*FA*) provided in the specifications (Jing & Zhendong, 2013). The detailed parameters are presented in Tables 4 and 5.

$$SA = \sum\left(P_i \times FA\right), \tag{1}$$

$$P_{\mathrm{m}} = \frac{SA_{\mathrm{AM}}}{SA_{\mathrm{OGFC}}} \times P_{\mathrm{a}}, \tag{2}$$

where SA is the specific surface area, m^2/kg, FA is the surface area coefficient with a diameter of 4.75 mm and an aggregate FA coefficient of 0.004, P_i is the percentage of the sieve residue for each aggregate grade, P_{m} is the asphalt mortar oil-sand ratio, %, SA_{AM} is the specific surface area of the aggregate in the asphalt mortar, m^2/kg, SA_{OGFC} is the specific surface area of the aggregates, m^2/kg, and P_{a} is the oil-stone ratio of the OGFC, %.

Table 4. Surface area coefficient *FA*

Mesh size, mm	16	13.2	9.5	4.75	2.36	1.18	0.6	0.3	0.15	0.075
Surface area coefficient *FA*	0.0041	–	–	0.0041	0.0082	0.0164	0.0287	0.0614	0.1229	0.3277

Table 5. Calculated oil-sand ratio of asphalt mortar

Oil-stone ratio of asphalt mixture	4.9%	5.1%	5.3%
Oil-sand ratio of asphalt mortar	35.1%	36.4%	37.8%

2. Macroscopic splitting fatigue test of OGFC

2.1. Test method

In this study, the hydrostatic moulding method was used to prepare cylindrical specimens with a diameter of 100 mm and height of 63.5 mm. Indirect tensile splitting fatigue tests were performed on OGFC specimens with varying oil-stone ratios, void fractions, and nominal maximum particle sizes.

The splitting test conditions included a temperature of 15 °C, loading rate of 50 mm/min, and termination condition defined as complete failure of the specimen.

The splitting strength was calculated according to Equation (3) in accordance with JTG E20-2011.

$$R_T = 0.006287 \frac{P_T}{h}, \tag{3}$$

where R_T denotes the splitting tensile strength, MPa, P_T is the maximum test load, kN, and h is the height of the specimen, mm.

The fatigue test was conducted at a temperature of 15 °C, using a controlled stress mode for loading. The loading frequency was 10 Hz, and a half-sine wave was applied. Three stress ratios (0.2, 0.3, and 0.4) were used as stress levels, and the test termination condition was specimen fracture. The fatigue equation is expressed as Equation (4) in accordance with JTG E20-2011.

$$\lg N_f = \lg K_m - n \lg \sigma, \tag{4}$$

where N_f is the fatigue life (time), σ represents the indirect tensile stress on the specimen, MPa, and K_m and n represent parameters of the fatigue equation.

2.2. Results

2.2.1. Results of OGFC macroscopic splitting fatigue test

The results of the splitting fatigue tests are shown in Table 6 and Figure 1. A larger K_m indicates better fatigue resistance, while a larger n value signifies a higher sensitivity of its fatigue life to the stress level.

The splitting strength and fatigue life of OGFC increased at higher oil-stone ratios. This is attributed to the additional asphalt film provided by higher oil-stone ratios, which enhances the bonding between aggregates. Conversely, both splitting strength and fatigue life showed a monotonic decrease with increasing void fractions. This is because a higher void fraction decreases the stability of the OGFC skeleton, significantly affecting its structural strength.

Similarly, splitting strength and fatigue life decreased at increasing nominal maximum grain sizes. The high void fraction, typical of OGFC mixes, may reduce durability and strength when larger particle-size aggregates are used. This is owing to the diminished compactness of the skeleton structure formed by larger particle sizes, which impacts the load-bearing capacity of the mix. These results are consistent with recent multiscale fatigue studies that identified a strong correlation between mixture compactness and fatigue resistance (Chen et al., 2023; Tan et al., 2024; Wu et al., 2024).

Table 6. Parameters of regression equation of OGFC splitting strength and life using different influencing factors

Parameter	Oil-stone ratio, %			Void rate, %			Nominal maximum particle size, mm		
	4.90	5.10	5.30	19	21	23	10	13	16
R_T, MPa	0.538	0.548	0.551	0.592	0.548	0.509	0.595	0.548	0.468
K_m	1224.616	1541.725	2824.881	2079.697	1541.711	1066.596	3040.885	1541.701	883.079
N	–2.708	–2.674	–2.504	–2.651	–2.674	–2.727	–2.511	–2.674	–2.588
R^2	0.993	0.993	0.988	0.993	0.993	0.995	0.993	0.993	0.989

a) logarithmic fits of OGFC fatigue life for different oil-stone ratios

b) logarithmic fits of OGFC fatigue life for different void fractions

c) logarithmic fits of OGFC fatigue life for different nominal maximum particle sizes

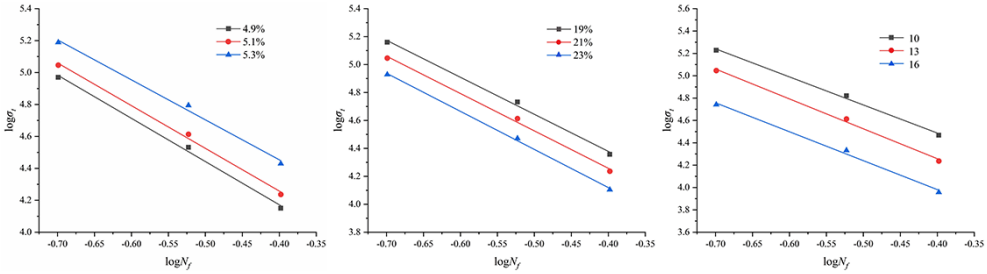

Figure 1. Logarithmic fit of open-graded friction courses (OGFC) fatigue life with different influencing factors

3. Material parameters

In this study, basalt was selected as the coarse aggregate owing to its linear elastic properties. Its constitutive equation is described by the generalized Hooke's law, with a modulus of elasticity of 40000 MPa and Poisson's ratio of 0.2 (Jing & Zhendong, 2013). Conversely, the asphalt mortar was modelled as a viscoelastic material with a modulus of elasticity of 400 MPa and Poisson's ratio of 0.3 (Jing & Zhendong, 2013). The Burgers model was selected as the viscoelastic intrinsic model for asphalt mortar (Figure 2).

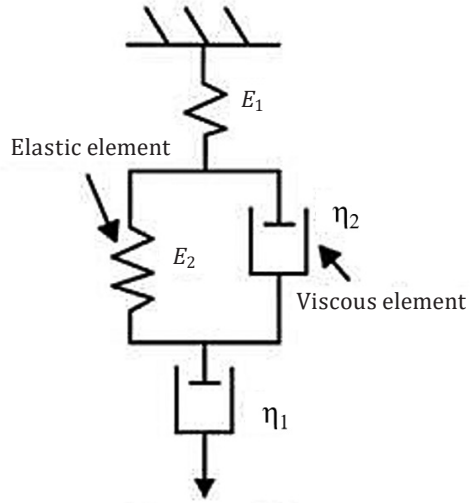

Figure 2. Burgers model

Based on the mechanical composition of the Burgers model, the creep equation is shown in Equation (5).

$$\varepsilon(t)=\sigma_0\left[\frac{1}{E_1}+\frac{1}{\eta_1}t+\frac{1}{E_2}\left(1-e^{-\frac{E_2}{2}}\right)\right], \tag{5}$$

where E_1 represents the instantaneous elastic modulus, MPa, E_2 – the delayed elasticity modulus, MPa, η_1 – the instantaneous coefficient of viscosity, and η_2 – the delayed coefficient of viscosity.

The four parameters of the Burgers model were converted into the Prony series. The elastic modulus was first transformed into the shear modulus, with the respective expressions shown in Equations (6) and (7):

$$G_1=\frac{E_1}{1+2\mu}, \tag{6}$$

$$G_2=\frac{E_2}{1+2\mu}, \tag{7}$$

where G_1 and G_2 represent the shear modulus, Pa, and μ represents the Poisson's ratio.

The relaxation modulus is obtained using the Laplace transform.

$$Y(t)=\frac{2G_1}{\alpha-\beta}\left[\left(\frac{G_2}{\eta_2}-\beta\right)e^{-\beta t}-\left(\frac{E_2}{\eta_2}-\alpha\right)e^{-\alpha t}\right], \tag{8}$$

where

$$\alpha = \frac{1}{2p_2}\left(p_1 + \sqrt{p_1^2 - 4p_2}\right),$$

$$\beta = \frac{1}{2p_2}\left(p_1 - \sqrt{p_1^2 - 4p_2}\right), \text{ and}$$

$$p_1 = \frac{\eta_1 E_1 + \eta_1 E_2 + \eta_2 E_1}{E_1 E_2},$$

$$p_2 = \frac{\eta_1 \eta_2}{E_1 E_2}.$$

The expressions for the shear modulus and relaxation modulus are given as

$$G(t) = 0.5Y(t) = G_\infty + G_0\left(g_1 e^{-\frac{t}{\tau_1}} + g_2 e^{-\frac{t}{\tau_2}}\right), \tag{9}$$

where

$$G_\infty = 0, G_0 = G_1,$$

$$g_1 = \frac{1}{\alpha - \beta}\left(\frac{G_2}{\eta_2} - \beta\right), g_2 = \frac{1}{\alpha - \beta}\left(\frac{G_2}{\eta_2} - \alpha\right),$$

$$\tau_1 = \frac{1}{\beta}, \tau_2 = \frac{1}{\alpha}.$$

Based on "Standard Test Methods of Bitumen and Bituminous Mixtures for Highway Engineering" (China Communications Press, 2011), the hydrostatic moulding method was selected in this study to prepare cylindrical asphalt mortar specimens with a diameter and height both of 100 mm. Uniaxial creep tests were conducted on asphalt mortar specimens with different oil-sand ratios at an indoor test temperature of 15 °C. Constant loads of 0.348, 0.315, and 0.289 MPa were applied to the top of the specimens with oil-sand ratios of 35.1%, 36.4%, and 37.8%, respectively. The mortar creep test results are shown in Figure 3, and the four parameters g_1, g_2, τ_1, and τ_2 of the Prony series were obtained by fitting the test curves. The specific parameters are listed in Table 7.

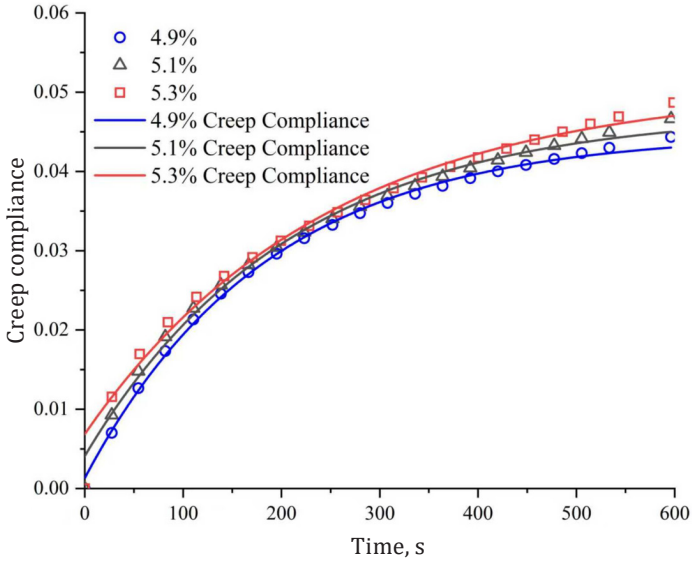

Figure 3. Fitting results of the mortar creep test

Table 7. Prony level parameters

Oil-stone ratios, %	g_1	g_2	τ_1	τ_2
4.9	0.066889	0.933111	734.2541	11.32127
5.1	0.03342	0.96658	1034.801	6.726472
5.3	0.001295	0.998705	1680.098	0.293622

4. Multiscale strategy

4.1. CT tomography test and digital image processing technology

OGFC specimens were scanned using a NanoVoxel-5000 CT scanner to capture a series of continuous two-dimensional (2D) images, as shown in Figure 4. By stacking and reconstructing these 2D images, the geometry and internal structure of the object were reconstructed in 3D space, generating interactive and visualised 3D graphics (Figure 5). The reconstructed 3D graphics were used to analyse statistically the distribution of OGFC aggregates, mortar, and voids. The analysis revealed that the percentage of void volume in the study area was 21.43%, which differed by only 0.47% from the actual measured voids of 20.96%, verifying the

reliability of the 3D model data. Furthermore, voids smaller than 2.36 mm accounted for approximately 8% of the total OGFC void fraction.

The extraction process for aggregates, mortar, and voids from the OGFC structure is shown in Figure 6.

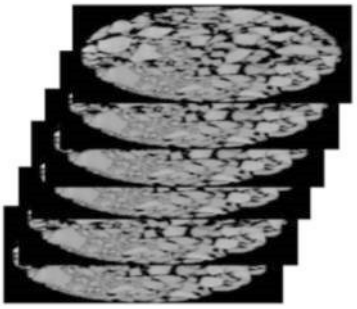

Figure 4. Multilayer pixel image stacking

Figure 5. Three-dimensional (3D) reconstruction of an OGFC specimen

a) regional extraction of aggregates

b) regional extraction of mortar

c) extraction of gap regions

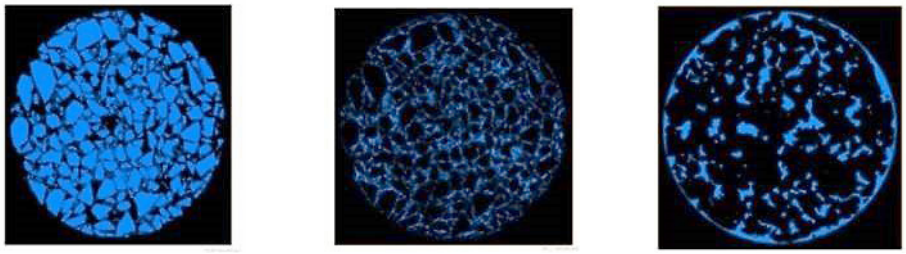

Figure 6. Extraction of aggregates, mortar, and voids in OGFC

After the CT 3D image of the asphalt mixture was segmented, it was further processed to generate a mesh model using the reconstruction software Avizo. The operational process is shown in Figure 7.

Figure 7. Avizo software meshing process

Based on the Poisson reconstruction algorithm, point-cloud data were utilised to reconstruct the surface mesh, and global optimisation methods were applied to improve model accuracy. A tetrahedral mesh was generated using the 3D reconstructed OGFC surface model described above. Based on a triangulation technique, the meshing method divides the surface into several smaller triangles. The meshing of the OGFC following 3D reconfiguration is illustrated in Figure 8. The mesh model was then exported in an INP file format for subsequent ABAQUS simulations.

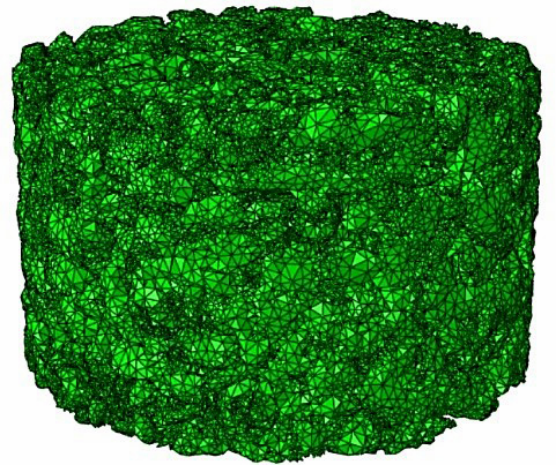

Figure 8. Mesh division of OGFC-13-21% specimen

4.2. Random aggregate dispensing algorithm

At the microscopic level, concrete is viewed as a three-phase composite material comprising aggregates, mortar, and voids. A Python script employing the Monte Carlo method was developed to simulate this process. The algorithm determines the boundary for aggregate generation, randomly selects the location and radius of aggregates within the boundary, and evaluates overlap conditions to generate aggregates shaped as forty-eight-sided polygons.

To ensure the aggregate particle size distribution aligns with practical requirements, the classical Fuller curve was applied (Shi et al., 2023), as described by the following equation:

$$P(d) = \sqrt{\frac{d}{d_{\max}}} \times 100\%, \tag{10}$$

where $P(d)$ represents the mass fraction of the aggregate with a particle size of <d, %, and d_{max} represents the maximum particle size of the aggregates, mm.

In the 3D model, the formulas for calculating the volume of coarse aggregates in each particle size range were established in accordance with JTG E20-2011 and are expressed as follows:

$$V_p\left[d_s, d_{s+1}\right] = \frac{P\left(d_s\right) - P\left(d_{s+1}\right)}{P\left(d\right) - P\left(d_{max}\right)} \times V_p \times V, \tag{11}$$

$$V_p = \frac{W_p}{\rho_p \times V}, \tag{12}$$

where $V_p[d_s,d_{s+1}]$ represents the volume of the coarse aggregate with a particle size of $[d_s,d_{s+1}]$, mm^3, d_{min} represents the minimum particle size of the coarse aggregates, mm, V_p – the volume fraction of the coarse aggregate generated, %, V – the total volume of the concrete specimen, mm^3, W_p – the total mass of coarse aggregate, g, and ρ_p – the apparent density of aggregate, g/cm^3.

Based on the grading, oil-stone ratio, and void fraction detailed in Table 3, the volume of mortar and voids < 2.36 mm, and the volumes of aggregates in the grade ranges of 2.36–6 mm, 2.36–4.75 mm, 4.75–9.5 mm, 9.5–13.2 mm, and 13.2–16 mm, could be obtained. Owing to algorithmic limitations, the mortar below 2.36 mm was set as a uniform entity with voids. Similarly, voids larger than 2.36 mm were approximated at 70% of their actual volume to enhance accuracy. The aggregate placement area was modelled as a cylinder with a diameter and height of 100 and 63.5 mm, respectively. Using the aggregate generation program, a random aggregate model with a 2 mm mesh size in the form of a forty-eight-sided polyhedron was created, as shown in Figure 9.

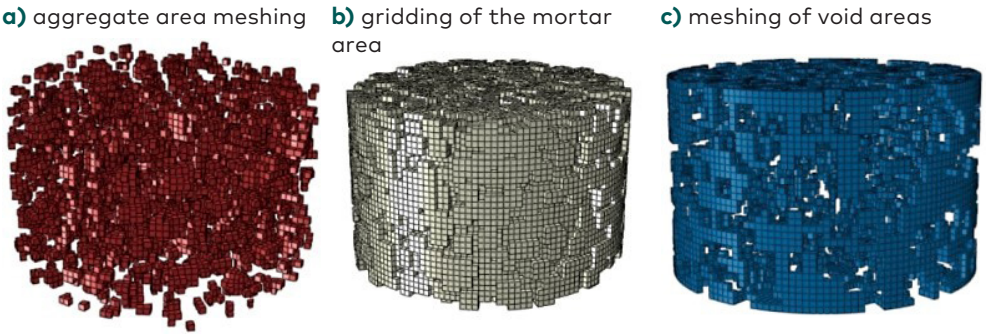

Figure 9. Aggregate, mortar, and void meshing in the OGFC random aggregate model

5. Finite element model

5.1. Experimental conditions

5.1.1. Splitting test conditions

In the macroscopic splitting test, the specimen was loaded with compression bars. However, the SOLD45 element, an 8-node solid element, was used during the modelling process. Consequently, the load was directly applied to the node group that comprised the upper and lower elements of the model, disregarding the interaction between the aggregate and asphalt emulsion interfaces. A homogeneous loading approach was adopted, replicating the loads observed in the macroscopic splitting tests.

Before conducting the analysis, boundary conditions were defined. The upper and lower boundaries of the model were set as loading surfaces consisting of nodal sets. For the loading surface of the specimen, the translational degrees of freedom in the x-, y-, and z-directions were fixed as UX = UY = UZ = 0. For the loading surface of the specimen, the translation in the x-direction was set to UX = 0.

A nonlinear finite element analysis was conducted using the incremental iteration method by adding loads for the iterative analysis. Specifically for this indirect tensile numerical simulation, the initial analysis set the total analysis incremental step to one, initial incremental step to 0.01, minimum incremental step to 1E–5, and the maximum incremental step to the total time of one. Based on the preliminary analysis, fixed incremental steps (0.01) were selected for a detailed analysis of the process.

5.1.2. Fatigue test conditions

The splitting results were imported into the FESAFE software program for fatigue analysis. The OGFC specimen served as the fatigue calculation object for the entire component. The final stress values obtained from the ABAQUS analysis were utilised as the fatigue loads with a loading frequency of 10 Hz, consistent with the indoor test conditions.

The newly established OGFC material database includes parameters such as the fatigue algorithm, elastic modulus, Poisson's ratio, and S–N curve measurement data. The selected fatigue algorithm was the stress fatigue life algorithm (Goodman), which is suitable for low-cycle fatigue life analysis. The S–N curve was obtained using macroscopic indirect tensile fatigue testing of the OGFC. The ODB result file generated by the FESAFE software program was imported into the ABAQUS software program for post-processing to generate a fatigue life cloud map, illustrating the distribution of unit and node fatigue life across the model.

Jiang and Ni (2017) employed the digital image correlation method to evaluate the deformation and strain of Marshall specimens during split fatigue testing of asphalt mixtures. The study identified a 40 mm × 40 mm square area at the specimen's centre as the primary region experiencing vertical and lateral deformation and tensile strain. Based on this, the fatigue life in the OGFC fatigue simulation was defined as the minimum fatigue life value of the 40 mm × 40 mm square area in the middle of the specimen, as shown in Figure 10.

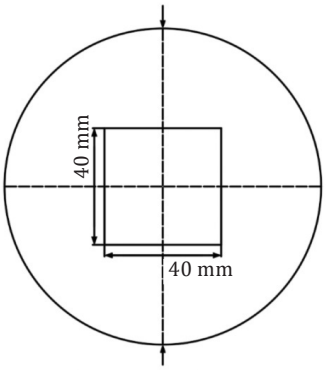

Figure 10. Fracture range of specimen in fatigue

5.2. Splitting fatigue virtual test of OGFC based on CT technology

5.2.1. Splitting virtual test of OGFC

In this study, OGFC-13-21 % was selected for finite element numerical splitting test simulations. The simulation results were compared with macroscopic splitting test data. The numerical simulations adopted the same loading boundary conditions as the macroscopic experiments. The simulation results are shown in Figure 11.

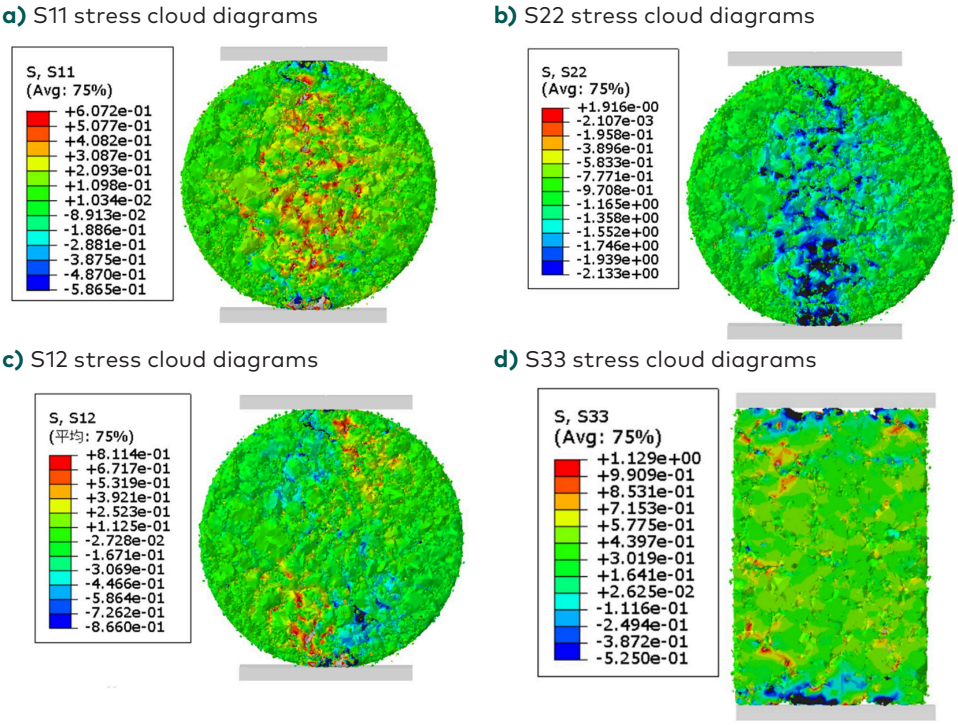

Figure 11. Stress cloud of the 3D reconstructed model

As evident from Figure 11, the simulation results align closely with the macroscopic experimental findings. The stress obtained from the numerical simulation was 0.607 MPa, representing a 10.7% difference from the macroscopic experimental splitting strength of 0.548 MPa. This consistency demonstrates that the 3D reconstruction model effectively reflects the asphalt mixture splitting-test process, highlighting a strong correlation between the two. Based on the observations in Figure 11, the distribution characteristics regarding the different stress cloud maps are described below:

1) The horizontal stress (S11) shows a horizontal band-like distribution due to the inhomogeneous distribution of the mortar and coarse aggregate. The mechanical properties of the mortar significantly affected the horizontal stress distribution.
2) The vertical stress (S22) shows a vertical-like band distribution along the coarse aggregate skeleton structure. The mortar's vertical stress cloud was relatively uniform because the embedded skeleton primarily influenced

the vertical stress distribution, while the coarse aggregate played a major supporting role.

3) The shear stress (S12) demonstrates a diagonal distribution along the direction of the long axis of the coarse aggregate at both ends. The stress within the coarse aggregate was uneven owing to the role of the embedded structure in resisting shear stress.
4) The Z-direction positive stress (S33) cloud shows that the stresses are distributed along the aggregate contact and that the distribution in the coarse aggregate is heterogeneous.

Stress changes in the two components were analysed to understand the roles of asphalt mortar and aggregate during the splitting test. A stress point was selected from each component in the model for evaluation. The trends of tensile and compressive stresses in the asphalt mortar and aggregate over time are shown in Figure 12.

a) Curves of S11 stress with time at asphalt mortar and aggregate

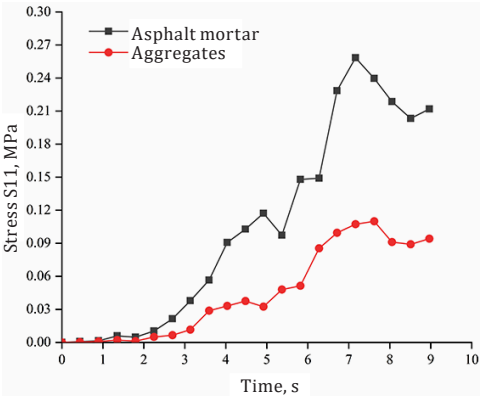

b) curves of S22 stress as a function of time at asphalt mortar and aggregate

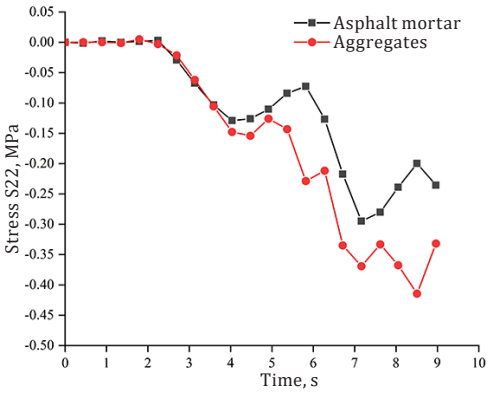

Figure 12. Plots of stress versus time curve of asphalt mortar and aggregate

Figure 12 illustrates that the maximum horizontal tensile stress occurs at the interface between the aggregate and the asphalt mortar, whereas the maximum vertical compressive stress is concentrated within the aggregate body. This indicates that under cyclic loading conditions, OGFC mixtures primarily experience fatigue failure when the horizontal tensile stress at the asphalt-aggregate interface exceeds the material's tensile limit. These findings confirm that fatigue cracking originates from interfacial stress concentration, which is consistent with the interface-level fatigue analyses reported by Mohamed et al. (2024).

5.2.2. Splitting fatigue virtual test of OGFC

The OGFC splitting results from the previous section were imported into FESAFE for further analysis, as shown in Figure 13. The simulation results align closely with the macroscopic experimental findings, with the errors of 9.0%, 9.7%, and 9.3% being within a 10% margin. This consistency confirms that the 3D reconstruction model effectively reflects the fatigue testing process of asphalt mixtures, indicating a strong correlation between the simulation and experimental results. The distribution of cloud maps at the three stress ratios is characterised as follows:

1) Nodes with lower cycle counts primarily exhibit a horizontal band distribution with uneven characteristics. This unevenness is due to the distribution state of the mortar, which significantly influences the fatigue life in the horizontal direction.
2) In the vertical direction, the coarse aggregate protects the mortar. Consequently, the number of nodes with low cycle counts is lower compared with those in the horizontal direction, reflecting the coarse aggregate's structural shielding effect.

a) Stress ratios of 0.2 **b)** Stress ratios of 0.3 **c)** Stress ratios of 0.4

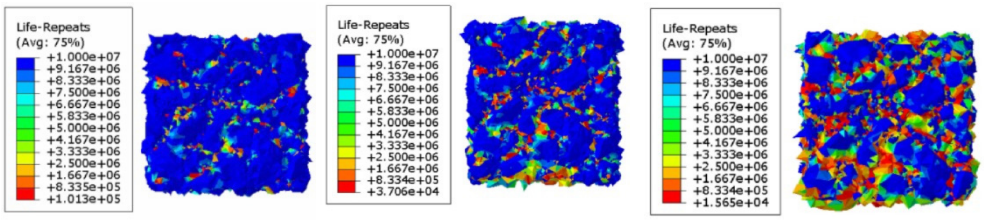

Figure 13. Lifetime clouds in a 40 mm × 40 mm square area

5.3. Microscopic splitting fatigue test of OGFC based on random aggregate algorithm

5.3.1. Microscopic splitting test of OGFC based on the random aggregate algorithm

To analyse the effects of oil-stone ratios, void fractions, and nominal maximum particle sizes on the performance of OGFC, the same test conditions were used to study the internal mechanical response of the material. The S11 stress clouds for OGFC under various conditions are shown in Figure 14. The S11 stresses of OGFC with different factors exhibit compressive stresses at both ends of the specimen and tensile stresses in the middle of the specimen. The maximum tensile stresses in the

cloud diagrams gradually increased at increasing oil-stone ratios. The maximum tensile stresses in the cloud diagrams gradually decreased with increasing void fractions and nominal maximum grain sizes.

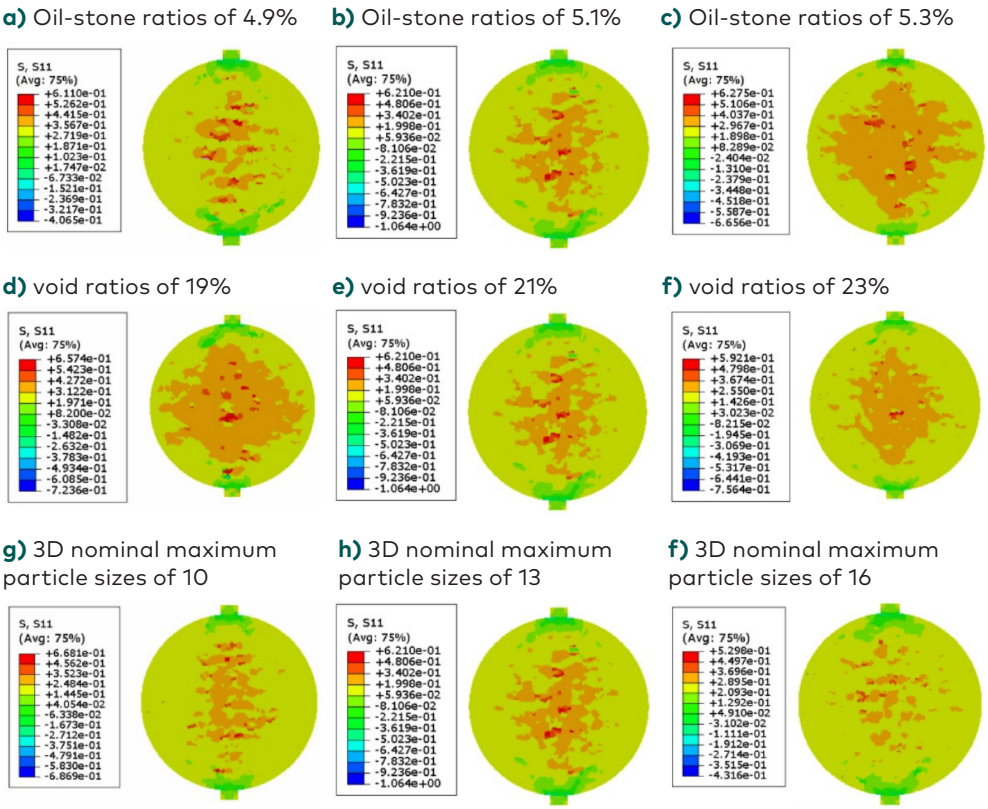

Figure 14. Splitting stress cloud maps at different influencing factors

A numerical analysis was performed on the OGFC splitting simulation results at varying oil–stone ratios, void fractions, and nominal maximum particle sizes. The distributions of the S11 stresses along the vertical loading axis are shown in Figure 15.

The analysis showed that the S11 stresses in the OGFC were compressive at both the top and bottom ends of the vertical loading axis, while tensile stresses were observed in the middle region. The points where tensile stresses began to emerge were approximately 10 cm from both the top and bottom ends, accounting for 80% of the total vertical loading axis length.

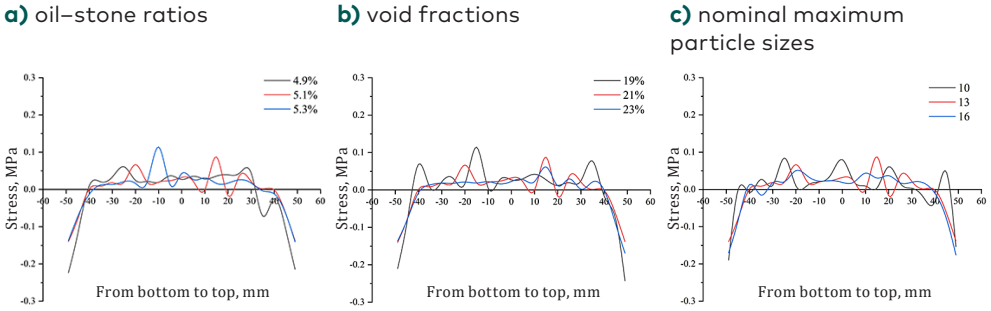

Figure 15. Stress distributions along the vertical axis of OGFC with different influencing factors

Figures 14a, 14b, 14c, and 15a show that the S11 stresses in the 3D model exhibit an overall increasing trend with higher oil-stone ratios. This is because (within a certain range) the splitting strength of the OGFC is primarily influenced by the filling state. As the oil-stone ratio increases, the mortar area expands, leading to a larger strain zone and more dispersed stress distribution. Consequently, the deformation area becomes broader, reducing the likelihood of localised damage. Figures 14d, 14e, 14f, and 15b show that the S11 stresses in the 3D model typically decrease at increasing void fractions. Comparable FEM analyses of stress evolution in porous asphalt mixtures conducted by Li et al. (2020) and Chen et al. (2023) also demonstrated that void connectivity and aggregate geometry strongly governed localised tensile stress concentrations and fatigue initiation, corroborating the present simulation trends. This is because (within a certain range) the splitting strength of OGFC with the same nominal maximum particle size but varying void fractions is predominantly affected by the fine aggregate distribution. As the void fraction increases, more fine aggregates fill the gaps between larger aggregate particles, diminishing their contact points. Under loading conditions, high-strain zones initially appear around the aggregate particles and then extend into the fine aggregate, creating embedded extrusion forces between aggregates. This reduces the stability of the skeleton structure.

As shown in Figures 14g, 14h, 14i, and 15c, the S11 stresses in the 3D model initially increase and then decrease as the nominal maximum particle size grows. Within a certain range, the number of contact points between skeleton particles decreases as the nominal maximum particle size increases. Additionally, larger particles occupy more space, reducing the compactness of the material. This results in a thinner mortar film, increased stress concentration, and deformation confined to smaller areas, ultimately weakening the strength of the sample.

5.3.2. Microscopic fatigue test of OGFC based on a random aggregate algorithm

Using the 3D virtual splitting model with different oil-stone ratios, void fractions, and nominal maximum particle sizes mentioned above, the fatigue characteristics of the OGFC were analysed using the FESAFE software program.

The lifetime stress-cloud diagram of the OGFC at a stress ratio of 0.4 is shown in Figure 16. The low-life regions in the cloud diagrams decrease as the oil-stone ratios, void fractions, and nominal maximum particle sizes increase. The low-life regions primarily appear around the aggregate.

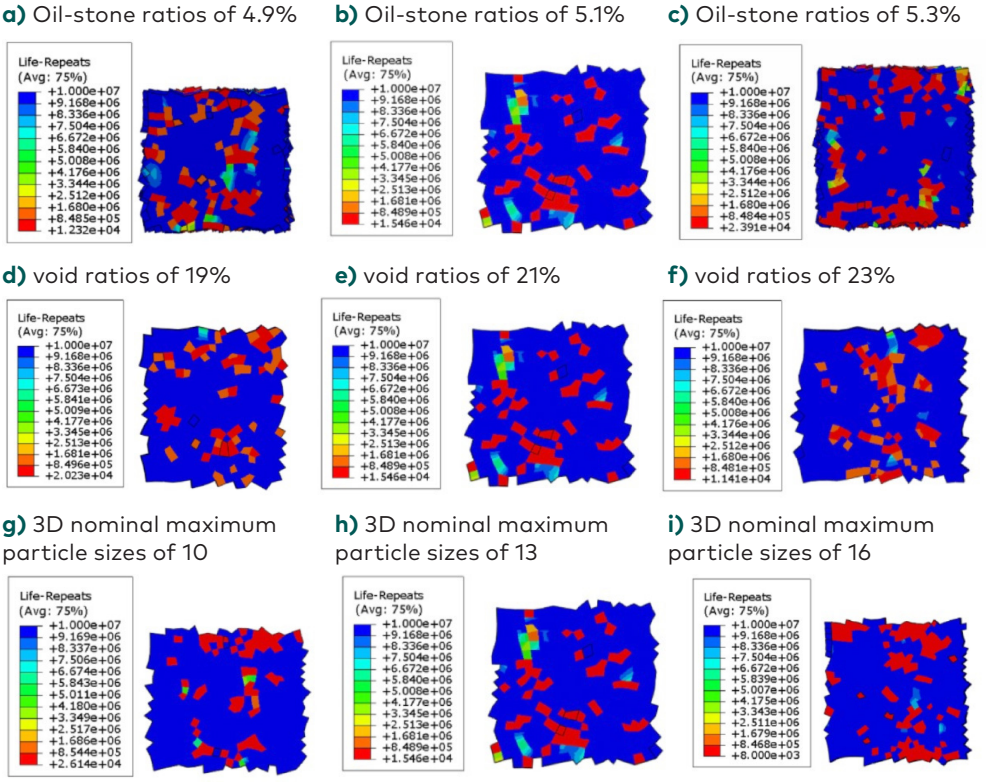

Figure 16. Cloud diagrams of fatigue life at different influencing factors

Figures 16a, 16b, and 16c illustrate an overall increasing trend in the fatigue life of the microfatigue test as the oil-stone ratio increases. This improvement occurred because as the oil–stone ratio increased, mortar film thickened, support ability of the asphalt mortar for the skeleton particles increased, and the contact force borne by the skeleton particles decreased, leading to an improvement in fatigue

life. Based on Figures 16d, 16e, and 16f, the fatigue life of the microfatigue test shows an overall decreasing trend at increasing void fractions. This is because the connection between the skeleton particles and asphalt mortar became weaker as the void fraction increased, resulting in a decrease in the strength of the specimen. This indicates that the void fraction, an inherent defect of OGFC, has a significant impact on the specimen's fatigue performance.

In Figures 16g, 16h, and 16i, the fatigue life of the microfatigue test shows a decreasing trend as the nominal maximum particle size increases. Larger particle sizes introduce more interfering particles, reducing the thickness of the asphalt mortar and its cohesion. Additionally, large particle sizes negatively affect the compactness of the specimen, further diminishing fatigue performance.

Conclusions

This study integrates macroscales and microscales to evaluate the effects of oil-stone ratios, void fractions, and nominal maximum particle sizes on the splitting strength and fatigue life of OGFC mixtures.

(1) Increasing the oil-stone ratio significantly enhances the structural integrity and energy dissipation capacity of OGFC mixtures by improving the mortar filling state, leading to higher splitting strength and fatigue life. Conversely, higher void fractions reduce the skeletal stability and interlocking forces of aggregates, resulting in lower mechanical performance. As the nominal maximum particle size increases, the overall skeleton becomes looser, decreasing cohesion within the asphalt-aggregate framework and weakening load-bearing capacity.

(2) The CT-based 3D reconstruction model of OGFC-13-21% effectively reproduced the macroscopic experimental results, with deviations of <11% for splitting strength and <10% for fatigue life. These results verify the accuracy and applicability of CT-based virtual modelling in predicting the mechanical response of porous asphalt mixtures. The analysis further revealed that fatigue failure predominantly initiates from the horizontal tensile stress concentration at the asphalt–aggregate interface, confirming the critical role of interfacial stress evolution in governing fatigue damage.

(3) By coupling experimental testing with 3D reconstruction and viscoelastic damage modelling, this study established a multiscale theoretical framework that links mixture composition parameters to fatigue life through interfacial stress evolution. This framework clarifies how structural compactness and stress-dispersion efficiency jointly govern fatigue deterioration, providing a new perspective beyond traditional phenomenological models.

Overall, this work bridges the macro-micro relationship of OGFC mixtures, revealing that interfacial mechanics are the intrinsic drivers of macroscopic fatigue behaviour. The findings offer a theoretical foundation for optimising gradation design and binder selection to enhance the durability and service life of open-graded asphalt pavements.

Acknowledgements

This study has been completed at the School of Civil Engineering in Shenyang Urban Construction Institute, School of Transportation and Geomatics Engineering in Shenyang Jianzhu University.

Funding

The research has been supported by the Key Project of Liaoning Provincial Department of Education [JYTZD2022170]. We hereby express our gratitude for their support.

Author Contributions

Conceptualization, BY; Data curation, BY; Formal analysis, BY and ZZ; Funding acquisition, LQ; Investigation, BY and ZZ; Methodology, CZ; Project administration, LQ; Resources, LQ and ZZ; Software, ZZ and CZ; Supervision, LQ; Validation, LQ and BY; Writing – original draft, LQ, BY and CZ; Writing – review and editing, LQ and CZ. All authors have read and agreed to the published version of the manuscript.

Disclosure Statement

No potential conflict of interest was reported by the authors.

REFERENCES

Chen, A., Airey, G., Thom, N. H., & Li, Y. (2023). Characterisation of fatigue damage in asphalt mixtures using X-ray computed tomography. Road Materials and Pavement Design, 24(4), 653–671. https://doi.org/10.1080/14680629.2022.2029756

Chen, D.-H., & Hugo, F. (1998). Full-scale accelerated pavement testing of Texas mobile load simulator. *Journal of Transportation Engineering-ASCE*, *124*(5), 479–490. https://doi.org/10.1061/(ASCE)0733-947X(1998)124:5(479)

China Communications Press. (2005). Highway engineering aggregate test procedures.

China Communications Press. (2011). Standard test methods of bitumen and bituminous mixtures for highway engineering.

Fakhri, M., Ghanizadeh, A. R., & Omrani, H. (2013). Comparison of fatigue resistance of HMA and WMA mixtures modified by SBS, *Procedia – Social and Behavioral Sciences*, *104*, 168–177. https://doi.org/10.1016/j.sbspro.2013.11.109

Fan, X., Liu, C., Lv, S., Ge, D., Liu, J., & Pan, Q. (2022a). Unified fatigue characterization of asphalt mixture under multi-field coupling condition: Stress state, frequency, and temperature. *SSRN Electronic Journal.* https://doi.org/10.2139/ssrn.4158348

Fan, X., Lv, S., Ge, D., Liu, C., Peng, X., & Ju, Z. (2022b). Time-temperature equivalence and unified characterization of asphalt mixture fatigue properties. *Construction and Building Materials*, *359*, Article 129118. https://doi.org/10.1016/j.conbuildmat.2022.129118

Hadley, W. O. (1993). Changes to the AASHTO guide for design of pavement structures. *Proceedings of the Pacific Rim Transtech Conference,* Volume II.

Hu, C., Ma, J., & Kutay, M. E. (2017). Three-dimensional digital sieving of asphalt mixture based on X-ray computed tomography. *Applied Sciences*, *7*(7), Article 734. https://doi.org/10.3390/app7070734

Ipekyol, A., Tortum, A., Rasouli, R., & Yazdani, M. (2022). Evaluating fatigue and crack resistance of asphalt mixture containing zinc tailing aggregates. *Case Studies in Construction Materials*, *17*, Article e01384. https://doi.org/10.1016/j.cscm.2022.e01384

Jian, J. (2011). Experimental research on anti-fatigue performance of OGFC mixture. *Journal of Chongqing Jiaotong University*, *30*(2), 254–257. https://doi.org/10.3969/j.issn.1674-0696.2011.02.17

Jiang, J., & Ni, F. (2017). Evaluation of fatigue property of asphalt mixtures based on digital image correlation method. *Journal of Southeast University*, *33*(2), 216–223. https://doi.org/10.3969/j.issn.1001-0505.2017.02.014

Jiang, Y., Deng, C., Xue, J., & Chen, Z. (2018). Investigation into the performance of asphalt mixture designed using different methods, *Construction and Building Materials*, *177*, 378–387. https://doi.org/10.1016/j.conbuildmat.2018.05.108

Jiang, H., Qin, S., Fu, J., Zhang, J., & Ding, G. (2021). How to model and implement connections between physical and virtual models for digital twin applications. *Journal of Manufacturing Systems*, *58,* 20–30. https://doi.org/10.1016/j.jmsy.2020.05.012

Jing, H., & Zhendong, Q. (2013). Micro-scale moisture damage characteristics in epoxy asphalt concrete. *Dongnan Daxue Xuebao (Ziran Kexue Ban)/Journal of Southeast University (Natural Science Edition)*, *43*(2), 355–359.

Kim, Y. R., Baek, C., Underwood, B. S., Subramanian, V., Guddati, M. N., & Lee, K. H. (2008). Application of viscoelastic continuum damage model-based finite element analysis to predict the fatigue performance of asphalt pavements. *KSCE Journal of Civil Engineering*, *12*(2), 109–120. https://doi.org/10.1007/s12205-008-0109-x

Li, T., Liu, P., Du, C., Schnittcher, M., Hu, J., Wang, D., & Oeser, M. (2020). Microstructural analysis of the effects of compaction on fatigue properties of asphalt mixtures. *International Journal of Pavement Engineering*, *23*(1), 9–20. https://doi.org/10.1080/10298436.2020.1728532

Li, X., Lv, X., Liu, X., & Ye, J. (2019). Discrete element analysis of indirect tensile fatigue test of asphalt mixture. *Applied Sciences*, *9*(20), Article 4363. https://doi.org/10.3390/app9204363

Liu, X., Jiang, Y., Wang, Z., Zhong, R. Y., Cheung, H. J. H., & Huang, G. Q. (2021). ImseStudio: Blockchain-enabled secure digital twin platform for service manufacturing. *International Journal of Production Research*, *61*(12), 3984–4003. https://doi.org/10.1080/00207543.2021.2003462

Lv, S., Wang, X.-y., Liu, C., & Wang, S. (2018). Fatigue damage characteristics considering the difference of tensile-compression modulus for asphalt mixture. *Journal of Testing and Evaluation*, *46*(6), Article 20170114. https://doi.org/10.1520/JTE20170114

Lv, S., Wang, Z., Zhu, X., Yuan, J., & Peng, X. (2023). Research on strength and fatigue properties of asphalt mixture with different gradation curves. *Construction and Building Materials*, *364*, Article 129872. https://doi.org/10.1016/j.conbuildmat.2022.129872

Ma, T., Zhang, Y., Zhang, D., Yan, J., & Ye, Q. (2016). Influences by air voids on fatigue life of asphalt mixture based on discrete element method. *Construction and Building Materials*, *126*, 785–799. https://doi.org/10.1016/j.conbuildmat.2016.09.045

Mackiewicz, P. & Szydło, A. (2019). Application of X-ray tomography to assess fatigue structural changes in asphalt mixtures. *Bulletin of The Polish Academy of Sciences-Technical Sciences*, *67*(2), 307–315. https://doi.org/10.24425/bpas.2019.128604

Manrique-Sanchez, L., Caro, S., & Kim, Y.-R. (2020). Coupled effects of aging and moisture on the fracture properties of Permeable Friction Courses (PFC). *International Journal of Pavement Engineering*, *23*(4), 972–984. https://doi.org/10.1080/10298436.2020.1784417

Mohamed, A. I. H., Li, X., & Wang, Z. (2024). Preliminary study on multi-scale modeling of asphalt mixtures using microstructure-based FEM. Materials, *17*(20), Article 5041. https://doi.org/10.3390/ma17205041

Muniandy, R., Selim, A.A., & Hassim, S. (2004). Effect of Malaysian cellulose oil palm fiber in the tensile cracking of stone mastic asphalt. *International RILEM Conference on Cracking in Pavements: Mitigation, Risk Assessment, and Prevention*, 265–272.

Peng, Y., Gao, H., Lu, X.-y., & Sun, L. (2020). Micromechanical discrete element modeling of asphalt mixture shear fatigue performance. *Journal of Materials in Civil Engineering*, *32*(7), Article 04020183. https://doi.org/10.1061/(ASCE)MT.1943-5533.0003246

Phanden, R. K., Aditya, S., Sheokand, A., Goyal, K. K., Gahlot, P., & Jacsó, Á. (2022). A state-of-the-art review on implementation of digital twin in additive manufacturing to monitor and control parts quality. *Materials Today: Proceedings*, *56*(1), 88–93. https://doi.org/10.1016/j.matpr.2021.12.217

Poulikakos, L. D., Pittet, M., Dumont, A.-G., & Partl, M. N. (2014). Comparison of the two-point bending and four point bending test methods for aged asphalt concrete field samples. *Materials and Structures, 48*, 2901–2913. https://doi.org/10.1617/s11527-014-0366-8

Shi, C., Yu, H., Qian, G., Li, X., Zhu, X., Yao, D., & Zhang, C. (2023). Research on the characteristics of asphalt mixture gradation curve based on Weibull distribution. *Construction and Building Materials*, *366*, Article 130151. https://doi.org/10.1016/j.conbuildmat.2022.130151

Song, W., Gong, H., Zeng, S., Cong, L., Sun, Y., Wu, H., & Huang, B. (2021). Field performance evaluation of open-graded asphalt friction courses: A survival data analysis. *Construction and Building Materials, 306*, Article 124745. https://doi.org/10.1016/j.conbuildmat.2021.124745

Song, W., Shu, X., Huang, B., Woods, M. (2016). Laboratory investigation of interlayer shear fatigue performance between open-graded friction course and underlying layer. *Construction and Building Materials*, *115*, 381–389. https://doi.org/10.1016/j.conbuildmat.2016.04.060

Su, Y., & Nikraz, H. (2022). New analytical-modelling method to interpret flexural bending fatigue response of asphalt mixture using the S-VECD theory. *International Journal of Pavement Engineering*, *23*(8), 2829–2845. https://doi.org/10.1080/10298436.2021.1873328

Sun, Y., Fang, C., Wang, J., Ma, Z., & Ye, Y.-J. (2018). Energy-based approach to predict fatigue life of asphalt mixture using three-point bending fatigue test. *Materials*, *11*(9), Article 1696. https://doi.org/10.3390/ma11091696

Tan, Z., Li, J., Leng, Z., Yin, B., Li, D., Zou, F., & Cao, P. (2024). Fatigue performance analysis of fine aggregate matrix using a newly designed experimental strategy and viscoelastic continuum damage theory. *Materials and Structures*, *57*(6), Article 130. https://doi.org/10.1617/s11527-024-02338-6

Wang, D., Ding, X., Gu, L., & Ma, T. (2018). Assessment model and virtual simulation for fatigue damage evolution of asphalt mortar and mixture. *Advances in Materials Science and Engineering*, *2018*, Article 9315463. https://doi.org/10.1155/2018/5904807

Wang, Z., Liu, D. Y., Hu, B., Zhu, C., & Luo, W. (2023). An improved regression model to predict fatigue life of asphalt mixes incorporating low to moderate RAP contents. *Construction and Building Materials*, *374*, Article 130904. https://doi.org/10.1016/j.conbuildmat.2023.130904

Wu, H., Huang, K., Song, W., & He, F. (2021). Characterizing the fatigue cracking behaviors of OGFC pavements using the overlay tester. *Construction and Building Materials*, *307*, Article 124979. https://doi.org/10.1016/j.conbuildmat.2021.124979

Wu, H., Ji, X., Song, W., Deng, Z., Zhan, Y., Zou, X., Li, Q. & He, F. (2024). Multi-scale analysis on fracture behaviors of asphalt mixture considering moisture damage. *Construction and Building Materials*, *416*, Article 135234. https://doi.org/10.1016/j.conbuildmat.2024.135234

Yu, H., Shen, S., Qian, G., & Gong, X. (2020). Packing theory and volumetrics-based aggregate gradation design method. *Journal of Materials in Civil Engineering*, *32*(6), Article 04020110. https://doi.org/10.1061/(ASCE)MT.1943-5533.0003192

Zhang, J., Huang, W., Hao, G., Yan, C., Lv, Q., & Cai, Q. (2020a). Evaluation of open-grade friction course (OGFC) mixtures with high content SBS polymer modified asphalt. *Construction and Building Materials 270*, Article 121374. https://doi.org/10.1016/j.conbuildmat.2020.121374

Zhang, J., Huang, W., Zhang, Y., Lv, Q., & Yan, C. (2020b). Evaluating four typical fibers used for OGFC mixture modification regarding drainage, raveling, rutting and fatigue resistance. *Construction and Building Materials*, *253*, Article 119131. https://doi.org/10.1016/j.conbuildmat.2020.119131